JOURNAL OF THE ROYAL SOCIETY Interface

CrossMark click for updates

J. R. Soc. Interface (2012) **9**, 3140–3155
doi:10.1098/rsif.2012.0479
Published online 15 August 2012

Epidermis architecture and material properties of the skin of four snake species

Marie-Christin G. Klein* and Stanislav N. Gorb

Functional Morphology and Biomechanics, Zoological Institute of the University of Kiel, Am Botanischen Garten 1-9, 24098 Kiel, Germany

On the basis of structural and experimental data, it was previously demonstrated that the snake integument consists of a hard, robust, inflexible outer surface (*Oberhäutchen* and β-layer) and softer, flexible inner layers (α-layers). It is not clear whether this phenomenon is a general adaptation of snakes to limbless locomotion or only to specific conditions, such as habitat and locomotion. The aim of the present study was to compare the structure and material properties of the outer scale layers (OSLs) and inner scale layers (ISLs) of the exuvium epidermis in four snake species specialized to live in different habitats: *Lampropeltis getula californiae* (terrestrial), *Epicrates cenchria cenchria* (generalist), *Morelia viridis* (arboreal) and *Gongylophis colubrinus* (sand-burrowing). Scanning electron microscopy (SEM) of skin cross sections revealed a strong variation in the epidermis structure between species. The nanoindentation experiments clearly demonstrated a gradient of material properties along the epidermis in the integument of all the species studied. The presence of such a gradient is a possible adaptation to locomotion and wear minimization on natural substrates. In general, the difference in both the effective elastic modulus and hardness of the OSL and ISL between species was not large compared with the difference in epidermis thickness and architecture.

Keywords: effective elastic modulus; nanoindentation; gradient materials; wear resistance; Reptilia

1. INTRODUCTION

Snakes are limbless reptiles that use their entire body for sliding locomotion. This supposes that the epidermis, especially that of the ventral body side, has to permanently endure friction forces. Because the epidermis is constantly in contact with the solid substrates, one can expect some specializations in the snake epidermis against abrasion [1]. Such specializations include layered organization of the epidermis, material properties of the epidermis and its surface microstructure.

Even though snakes from different lineages have different body size, scale dimension, body shape and body mass [2], previous morphological examinations have shown that their epidermis basically consists of six layers overlying the dermis [3,4]. The following epidermis layers from the outer scale surface towards the dermis are known (figure 1*c*): (i) the *Oberhäutchen*, (ii) β-layer, (iii) mesos-layer, (iv) α-layer, (v) lacunar tissue and (vi) clear layer. On the basis of structural data, it has been previously assumed that the epidermis of snakes consists of a hard, robust, inflexible outer surface (*Oberhäutchen* and β-layer) and soft, flexible inner layers (α-layers) [3,6,9–19]. In our previous study [1], we used the nanoindentation technique, which has been previously used to evaluate local mechanical properties of various biological materials [5,20,21]. Both the effective elastic modulus (EEM) and hardness (HD) of the outer and inner epidermis layers of the ventral scales of the Kenyan sand boa (*Gongylophis colubrinus*) exuvium were characterized [1]. The results obtained provided evidence for the presence of a gradient in material properties in the *G. colubrinus* skin.

Although it is known that the epidermis of snakes consists of six main layers, there has not been a single study comparing the cross-section architecture of these layers between different snake species inhabiting different environments and preferably using different modes of locomotion. From previous studies [10, 22–29], it is known that between different snake species the scale surface microstructure can vary significantly even between representatives of the same family. That is why these microstructures have been used for taxonomic purposes, but with a limited success. Scale microstructures vary between dorsal, lateral and ventral body regions within a single species [1,30]. In a few experimental studies, these microstructures have been shown to influence frictional properties of different skin regions [30–32]. Furthermore, depending on function, the scale surface microstructure may also vary within one body region. For instance, the surface structure of the infrared imaging pit organ scales reveals indistinguishable geometrical parameters in contrast

*Author for correspondence (mklein@zoologie.uni-kiel.de).

Received 15 June 2012
Accepted 24 July 2012

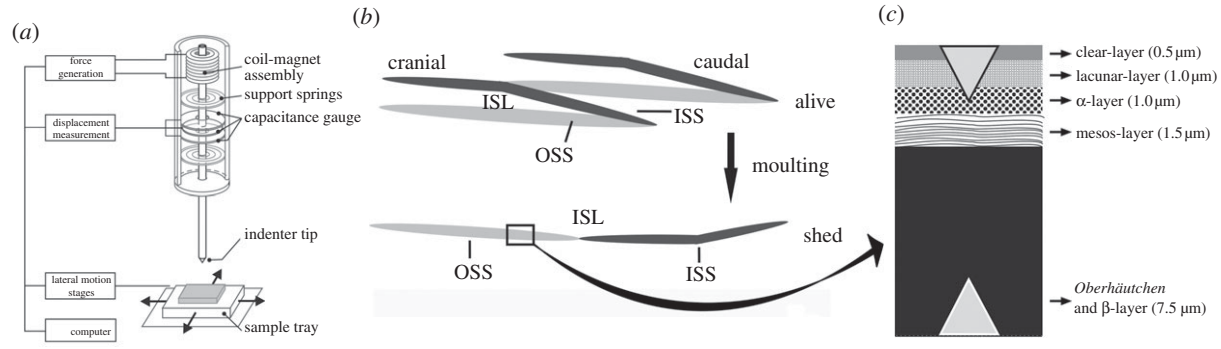

Figure 1. (*a*) Schematic diagram of the indentation system set-up with the coil-magnet assembly for load application, the capacitive displacement sensor and the indenter shaft support springs [5]. (*b*) Schematic drawing of the epidermis on scale level. The black square illustrates the skin part that was tested. (*c*) Diagram of the cross section of the snake integument (after [6–8], and the present study). Triangles indicate the indentation depth undertaken in this study. ISL, inner scale layers; ISS, inner scale surface; OSS, outer scale surface. Figure 1*a* was adapted with permission from Barbakadze *et al.* [5]. Adapted with permission from Klein *et al.* [1].

to the surrounding surface and other body scales. The characteristic array of nanopits, plate dimensions and terrace-like microstructure exists in all snakes with infrared imaging capability independent of species and age. It is suggested that both the spacing and dimensions of these structures play an important role in the ability to detect and enhance the absorption of infrared radiation [33–38].

In sliding contacts, local stress concentrations on the surface lead to material fatigue and failure. The surface is more effective against abrasion wear, if it has a gradient in material structure and properties, because it leads to a more uniform stress distribution, and thus to the minimization of local stress concentrations [39–42]. A hard, inflexible surface material easily forms cracks under pressure, whereas a soft flexible system will be easily worn off under shear stress. As we have previously assumed [1], the gradient in material properties from a stiff surface to a soft depth will improve wear resistance in snake skin by combining the advantages of stiffness and flexibility.

The exuvium surface geometry of shed epidermis does not differ from that of a live animal (M.-C. G. Klein 2010, personal observation). In a living snake, each scale has two exposed sides (called hereafter the outer scale layer (OSL)): (i) the outer scale surface (OSS)—which is in contact with the substrate—and (ii) the inner scale surface (ISS)—which is in contact with the following scale. Both the OSS and ISS are composed of the six cell layers mentioned above. The epidermis side that is facing the *stratum germativum* is here called the inner scale layer (ISL), which becomes exposed after the skin has been shed (figure 1*b*).

The aim of this study is to understand structural and mechanical properties of the skin as possible adaptations to a limbless way of life. For this purpose the structure of epidermal layers was compared between snake species inhabiting different environments, moving on different substrates and using different locomotion types. The local material properties of the OSL and ISL of the ventral exuvium surface within a species, as well as between the four selected species were compared. Exuvia of the king snake (*Lampropeltis getula californiae*), the Brazilian rainbow boa (*Epicrates cenchria cenchria*), the green tree python (*Morelia viridis*) and the previously studied Kenyan sand boa (*G. colubrinus*) were used in this study.

Lampropeltis getula californiae is a relatively fast-moving terrestrial snake that inhabits woods, scrubs and cultivated land from the southeast of the United States to Mexico. It is a slim snake with a round to square body cross section. It mostly uses lateral undulation to move forward. *Epicrates cenchria cenchria* is a generalist, which means it inhabits trees, water, rocks and terrestrial habitats in tropical rainforests. It is a relatively heavy snake with a round body cross section. It employs lateral undulation and rectilinear locomotion. *Morelia viridis* is an exclusively arboreal snake inhabiting tropical rainforests in Papua New guinea and Australia. Like all typical arboreal snakes, it has a laterally flattened body cross section. It does not move much, except when it catches prey. During prey capture, it catapults its body towards the prey and then pulls itself back with the help of its tail, which remains attached to the tree. *Gongylophis colubrinus* inhabits the Kenyan desert and moves either through the sand or on it. During locomotion, its epidermis is in continuous sliding contact with highly abrasive sand particles. The way it moves in sand has not yet been studied, but on the sand, it uses mostly lateral undulation [2,43–45].

2. MATERIAL AND METHODS

2.1. Animals

Adult female exuvia of *G. colubrinus*, *L. g. californiae* and *E. c. cenchria* (kept at the University of Kiel, Germany), and *M. viridis* (reared at the Zoo Leipzig GmbH, Germany) were studied. *Gongylophis colubrinus* was reared on desert sand white (Hobby Terrano, Gelsdorf, Germany) in a 100 × 50 × 60 cm (width × height × depth) terrarium. *Lampropeltis getula californiae* was reared on bark mulch (Plantania, Florasan GmbH, Kempen, Germany) mixed with *Sphagnum* moss in a 120 × 50 × 60 cm terrarium. *Epicrates cenchria cenchria* was reared on the same substrate as *L. g. californiae* in a 180 × 100 × 90 cm terrarium.

Morelia viridis was reared in a $210 \times 220 \times 130$ cm terrarium with plants and branches as the substrate.

2.2. Nanoindentation

The experimental set-up was the same as described in Klein *et al.* [1], in which the Nano Indenter SA2 (MTS Nano Instruments, Oak Ridge, TN, USA) equipped with the continuous stiffness measurement (CSM) technique, allowing testing of soft biological tissues or gels [21,46], was used for dynamic indentation tests. Nanoindentation is a technique to measure the mechanical properties of small volumes of material [47–49]. From obtained force–displacement curves, both HD and elasticity modulus of materials can be determined [47] at penetration depths ranging from several hundred nanometres to few dozens of micrometres [21]. HD and elasticity were acquired from the following equations [47,50]:

$$H = \frac{p_{\max}}{A_c}, \tag{2.1}$$

where H is hardness, $P_{\max}$ is the maximal load and A_c is the contact area,

$$E_{\text{eff}} = \frac{\sqrt{\pi}}{2} \cdot \frac{S}{\beta \cdot \sqrt{A_c}}, \tag{2.2}$$

with E_{eff} being the reduced (or effective) elastic modulus, β, the correction factor for the indenter form, and S, the contact stiffness. Owing to the variation of material structure in the depth of biological samples, mechanical properties might fluctuate considerably with depth [21]. Therefore, the CSM method was applied, which allows measurements of mechanical properties as a function of depth [21,47]. In our previous work, we successfully applied this method for mechanical characterization of biological samples such as insect cuticle [5,20], plant cuticle [21] and snake skin [1].

2.3. Sample preparation and test procedure for nanoindentation

Exuvia scales from *G. colubrinus*, *L. g. californiae*, *E. c. cenchria* and *M. viridis*, were cut from ventral, mid-body regions, attached to an aluminium sample holder, as described in Klein *et al.* [1] in one of the two ways: (i) the OSL (*Oberhäutchen*/β-layer) of the OSS facing the indenter tip; (ii) the ISL (clear-layer) of the OSS facing the tip. This way the mechanical properties into the direction perpendicular to the surface and to the keratin fibres were obtained. The results acquired from this experimental setup are relevant to the way how the forces are acting on the snake skin during locomotion [1]. Three to six individual scales were tested. A total of 25–50 individual indentations on the posterior margin of the scale were carried out on each individual scale. The samples were loaded under constant strain rate conditions with a rate of $0.02\ \text{s}^{-1}$ to a maximum penetration depth of 10 µm (for further details see [1]). To ensure proper surface detection, the procedure described in Deuschle *et al.* [46] was used.

2.4. Scanning electron microscopy of cross sections

Ventral scales of *G. colubrinus*, *L. g. californiae*, *E. c. cenchria* and *M. viridis* exuvia were cut and mechanically fixed on a specimen holder in a vertical position, so that the fractured material could be examined in the cross-fracture. The fracture was produced by cutting over the fixed sample using either a razor blade or very sharp scissors. Samples were then sputter-coated using the internal sputter of a Gatan ALTO 2500 Cryo system (Abingdon Oxon, UK) with gold–palladium (6 nm thickness and a rate of 1 : 9). The samples were observed at room temperature, using a Hitachi-S4800 (Tokyo, Japan) scanning electron microscope (SEM) at an accelerating voltage of 2–5 kV.

2.5. Scanning electron microscopy of the scale surface

Exuvia (5×10 mm pieces) of ventral, dorsal and lateral scale regions of *G. colubrinus*, *L. g. californiae*, *E. c. cenchria* and *M. viridis* were cut and mechanically fixed on specimen holders in a horizontal position, with either the OSS or the ISS pointing upwards, so that the scale microstructure could be examined. Samples were also sputter-coated with gold–palladium (10 nm thickness and a rate of 1 : 9), using the Leica EM SCD 500 (Wetzlar, Germany) and observed in the SEM, as described before.

3. RESULTS

3.1. Morphological examination of the scale surface

The study of the exuvia using the SEM revealed that the ventral scale microstructure varies between the four snake species. The OSS of the dorsal, ventral and lateral scales of *G. colubrinus* and *L. g. californiae* bear strap-shaped cuticle cells, which exhibit round pits (table 1 and figure 2). The cells of the ventral, lateral and dorsal scales of *E. c. cenchria* change from polygonal to strap-shaped from the caudal to cranial part of the scale. The cells of the ventral and lateral scales of *M. viridis* change from polygonal to strap-shaped from the caudal to cranial part of the scale. The dorsal cells of *M. viridis* are strap-shaped in which denticulations create polygonal boundaries. Both polygonal- to strap-shaped cell types exhibit round pits (table 1 and figure 2).

The epidermis of *G. colubrinus* (figure 2*b*,*c*) shows a variation in the scale microstructure, when comparing the ventral and lateral sides of the body (figure 2*b*) with the dorsal one (figure 2*c*). Cells of all scale types (ventral, lateral and dorsal) have caudal elevations and random denticulations with irregular, round pits from the cranial to central part of the scale. However, in contrast to the dorsal scales bearing denticulations aligned in comb-like rows running perpendicular to the longitudinal body axis, the exposed parts of both lateral and ventral scales are relatively smooth, with little to no microstructure [1]. The microstructure that can sometimes be observed on the centre to caudal part of the ventral and lateral scales looks like an

Table 1. Morphological details of the ventral, lateral and dorsal scales in the snake species studied: *G. colubrinus* (*G. c.*), *L. g. californiae* (*L. g. c.*), *E. c. cenchria* (*E. c. c.*) and *M. viridis* (*M. v.*).

	ventral scales (OSS)	lateral scales (OSS)	dorsal scales (OSS)	cross sections
G. c.	— cells strap-shaped *cranial to centre*: caudal elevations and random denticulations (mean: 500 × 300 nm (length × width)) — irregular, round pits (mean diameter: 90–140 nm) *centre to caudal*: — little to no microstructure	— cells strap-shaped — *cranial to centre*: caudal elevations and random denticulations (mean: 500 × 300 nm (length × width)) — irregular, round pits (mean diameter: 90–140 nm) *centre to caudal*: — little to no microstructure	— cells strap-shaped — *cranial to centre*: caudal elevations and random denticulations (mean: 500 × 300 nm (length × width)) — irregular, round pits (mean diameter: 90–140 nm) *centre to caudal*: — denticulations in comb-like rows perpendicular to longitudinal body axis — central ridge	General: layers are dense and differentiated (20 μm width). From OSL to ISL: (i) dense cell layers with perhaps granular inclusions; (ii) less dense, big, round, thick disks; (iii) flat, frayed, elongated cells; (iv) one clearly separate cell layer. — Layers (ii) and (iii) loosely joined
L. g. c.	— cells strap-shaped *cranial to centre*: — cells with caudal elevations and random denticulations (mean: 350 × 350 nm (length × width)) — round pits (mean diameter: 100 nm) *centre to caudal*: — slightly sharp, relatively long and regular, densely packed denticulations (mean: 3 μm × 800 nm (length × width)), — longitudinal pits (mean: 400 × 100 nm (length × width)) between denticulations	— cells strap-shaped *cranial to centre*: — cells with caudal elevations and random denticulations (mean: 350 × 350 nm (length × width)) — round pits (mean diameter: 100 nm) *centre to caudal*: — slightly sharp, relatively long and regular, densely packed denticulations (mean: 3 μm × 800 nm (length × width)), — longitudinal pits (mean: 400 × 100 nm (length × width)) between denticulations	— cells strap-shaped *cranial to centre*: — spiky, small, irregular denticulations (mean: 700 × 300 nm (length × width)) — small round pits (mean diameter: 250 nm) *centre to caudal*: — spiky, large denticulations (mean: 2.23 μm × 600 nm (length × width)) — large, irregular and round pits (mean diameter: 400 nm)	General: Loosely packed cells (9 μm). from OSL to ISL: — heterogeneous β-layer (5 μm) with fibres (mean diameter: 400–600 nm) in first 2–3 μm — three to four single cell layers with clearly flattened, elongated cells, joined loosely to a very thin inner layer part
E. c. c.	— cells change from polygonal- to strap-shaped *cranial to centre*: — small, regular denticulations (mean: 400 × 550 nm (length × width)) — round regular pits (mean diameter: 300 nm) *centre to caudal*: — denticulation pattern, without elevations (mean: 10 × 1.9 μm (length × width)) — long longitudinal grooves and round regular pits (mean diameter: 120 nm)	— cells change from polygonal- to strap-shaped from caudal to cranial *cranial to centre*: — small, regular denticulations (mean: 400 × 550 nm (length × width)) — round regular pits (mean diameter: 300 nm) *centre to caudal*: — denticulation pattern, without elevations (mean: 10 × 1.9 μm (length × width)) — long longitudinal grooves and round regular pits (mean diameter: 120 nm)	— cells change from polygonal- to strap-shaped from caudal to cranial *cranial to centre*: — small, regular denticulations (mean: 400 × 550 nm (length × width)) — round regular pits (mean diameter: 300 nm) *centre to caudal*: — denticulation pattern, without elevations (mean: 10 × 1.9 μm (length × width)) — long longitudinal grooves and round regular pits (mean diameter: 120 nm)	General: Spongy, fraying, dense cells (40 μm). Spongy, flattened, elongated cells layers, which tend to fray quite intensely. The cells are densely packed throughout the epidermis and seem to be constructed like a fibre composite.

(*Continued.*)

Table 1. (*Continued.*)

	ventral scales (OSS)	lateral scales (OSS)	dorsal scales (OSS)	cross sections
M. v.	— cells change from polygonal- to strap-shaped from caudal to cranial *cranial to centre:* — regular, dense, round pits (mean diameter: 400 nm) *centre to caudal:* — regular, finger-like denticulations (mean: 1.5 µm × 700 nm (length × width)) — few round, irregular pits (mean diameter: 150 nm) in-between	— cells change from polygonal- to strap-shaped from caudal to cranial *cranial to centre:* — regular, dense, round pits (mean diameter: 400 nm) *centre to caudal:* — regular, finger-like denticulations (mean: 1.5 µm × 700 nm (length × width)) — few round, irregular pits (mean diameter: 150 nm) in-between	— cells are strap-shaped in which denticulations create polygonal boundaries *cranial to centre:* — large, dense, round pits (mean diameter: 400 nm) *centre to caudal:* — short, spiky denticulations (mean: 450 × 200 nm (length × width)) — large, dense, round pits thin (mean diameter: 400 nm) in-between	General: Cell types specifically merge to one mass (12 µm). From OSL to ISL: — two to three cell layers can be distinguished in the β-layer — OSL dense, followed by bloated, flattened cells that are joined loosely to a layer of frayed cells. — seamless transition from meso- to α-layer

imprint of the cuticle cells with long longitudinal furrow-like lines arranged on top of the cells, and round, small grooves in-between.

Ventral and lateral scale microstructure of *L. g. californiae* consists of rather sharp, relatively long, regular, densely packed denticulations with longitudinal pits between denticulations in the caudal part of each scale (figure 2*e*). Similar to *G. colubrinus*, *L. g. californiae* has cells on the ventral and lateral scales with caudal elevations, random denticulations and round pits from the cranial to central part of the scale. The dorsal scales of *L. g. californiae* exhibit spiky, large denticulations with large, irregular and round pits from the caudal to central part of the scale (figure 2*f*), and spiky, small, irregular denticulations with small round pits from the centre to the cranial scale region.

Dorsal (figure 2*i*), lateral and ventral (figure 2*h*) scales of *E. c. cenchria* have a similar microstructure, with a pattern of large, almost embedded denticulations without elevations and cells with elongated longitudinal grooves and round regular pits from the caudal to central scale part. In the cranial scale region, the microstructure changes to small, regular denticulations with round regular pits.

Morelia viridis is an arboreal snake with a slim and laterally flattened body. The lateral and ventral (figure 2*k*) scale microstructures are almost the same. The caudal to central scale region exhibits regular, finger-like denticulations with a few round, irregular pits in-between. Regular, dense, round pits are seen from the centre to cranial scale part. The dorsal scales (figure 2*l*) exhibit densely packed, large round pits. The denticulations of the dorsal scales are more slender and short, in contrast to the ventral and lateral scales.

The ISS of both *G. colubrinus* and *L. g. californiae* exhibits denticulations pointing towards the caudal direction, presumably interacting with the OSS denticulations that also point to the caudal direction. Similar structures were found, not only on the ventral, lateral and dorsal scales, but also on the ventro-lateral and dorso-lateral scales, which create the transition between body regions. The ISS of both *E. c. cenchria* and *M. viridis* reveal the same structures as the cranial to centre part of the OSS.

3.2. Morphological examination of the cross sections

Cross sections (table 1 and figures 3–6*b*) of exuvia were examined using SEM. The general composition of layers of the snake epidermis is well known, but layers vary in thickness in different species, presumably depending on environmental demands. Although the exact identification of specific layers is difficult in exuvia, the SEM examinations revealed that the layer thickness and architecture are different in the four species studied. The following description will start from the OSL. The OSL of the *G. colubrinus* (figure 3) exuvium (*ca* 20 µm thick), in general, bears layers that are clearly cut and densely packed. The first 3 µm of the *Oberhäutchen* and β-layer are extremely dense and have granular inclusions embedded, which are not found in the layers underneath (figure 3). The rest of

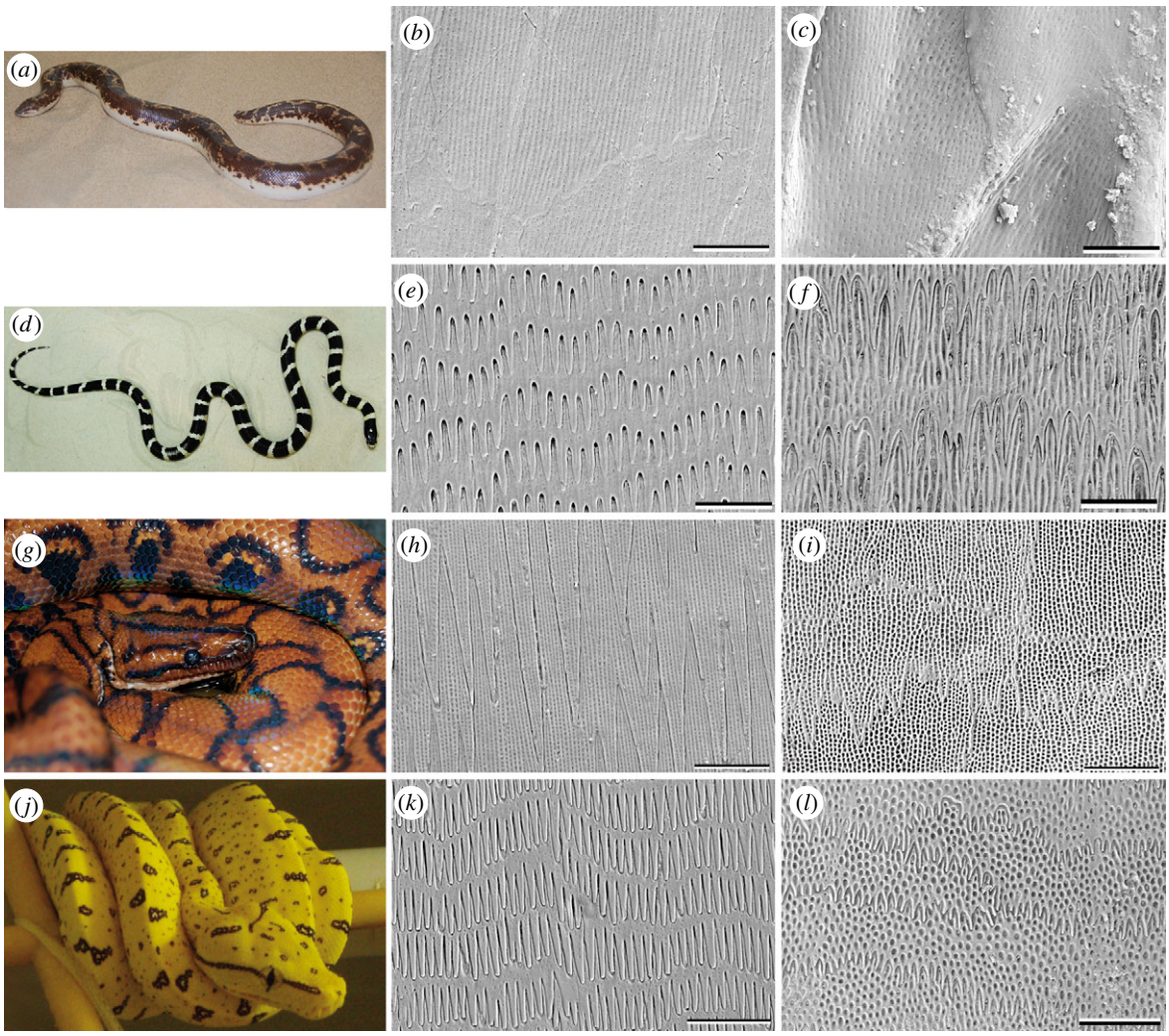

Figure 2. Overview of the four model snake species studied. (*a*,*d*,*g*,*j*): animals. (*b*,*c*,*e*,*f*,*h*,*i*,*k*,*l*): SEM images illustrating the microstructure of the *Oberhäutchen* on the caudal outer scale surface of the ventral (*b*,*e*,*h*,*k*) and dorsal (*c*,*f*,*i*,*l*) scales. (*a*–*c*) *G. colubrinus*; (*d*–*f*) *L. g. californiae*; (*g*–*i*) *E. c. cenchria*; (*j*–*l*) *M. viridis*. (Online version in colour.)

the β-layer exhibits relatively flat, densely packed cells. These two layer types seem to be joined loosely by fibre-like structures. The mesos-layer consists of approximately four of the typical single cell layers. The layer following the mesos-layer also consists of dense cells, although not as dense as the β-layer. The cells are small and flat. Differences between the α-layer and the lacunar tissue are difficult to make out. The clear-layer is clearly visible and differentiated as a one-cell layer.

The exuvium of *L. getula californiae* (figure 4) is about 9 μm thick. The exuvium exhibits fibres (diameter: 400–600 nm) embedded in the outer 2–3 μm of the very thick (5 μm) β-layer. The fibres are oriented at an angle of 15° to the scale surface in caudal direction. Such fibres were not observed in the other three species studied. The cells of the β-layer are very homogeneous. This layer is followed by flattened cells and joined loosely to a very thin inner layer part. Differences between the α-layer and the lacunar tissue are difficult to make out and the clear layer is not identifiable.

The cell layers of *E. c. cenchria* (figure 5; *ca* 40 μm thick) tend to wear quite intensely, especially the *Oberhäutchen* and β-layer. The first layer that can be distinguished when looking at the OSS is a single, shrivelled cell layer that is tightly connected to the next, thicker layer. This single-cell layer may still be the differentiated *Oberhäutchen*. The cells of the following layers are densely packed and resemble a fibre composite material. The β-layer is very thick, making up almost two-thirds of the entire exuvium. Almost, all the four single-cell layers of the mesos-layer can be distinguished. Differences between the α-layer, lacunar tissue and clear-layer are difficult to make out.

Morelia viridis (figure 6) has an exuvium (*ca* 12 μm thick) in which the cell types superficially merge into one mass. It is possible to distinguish at least two cell layers within the β-layer. The first one-third of the β-layer is densely packed. The cells of the second one-third look like flattened, spongy cells, which are followed by even flatter cells. The mesos-layer cannot clearly be distinguished because of the flatness of previous cells. The layer following both the β-layer and mesos-layer also consists of densely packed cells, and single cells can be distinguished in some areas. Differences between the α-layer and the lacunar tissue are difficult to make out, and the clear layer is not identifiable.

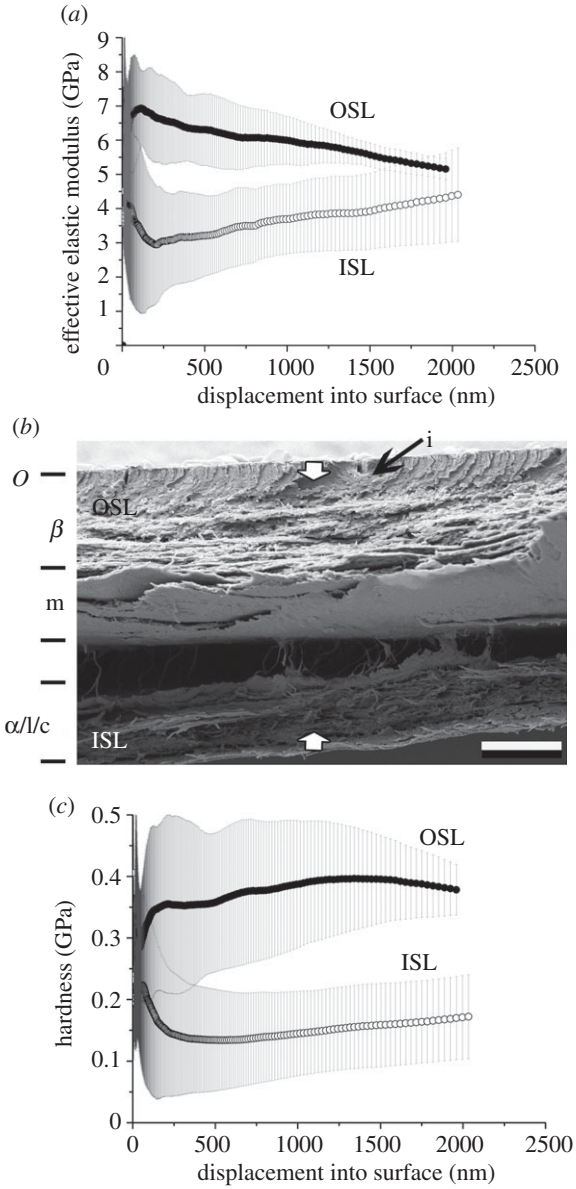

Figure 3. *Gongylophis colubrinus*. Results of nanoindentation measurements for both the OSL and ISL in relation with the cross-section architecture. (*a*) EEM versus displacement, (*b*) cross-section and (*c*) HD versus displacement. The error bars denote standard deviations. OSL, outer scale layers; ISL, inner scale layers; i, inclusions. The arrows indicate the indentation depth of 2 µm. *O*, *Oberhäutchen*; *β*, β-layer; m, mesos-layer; *α*, α-layer; l, lacunar tissue; c, clear-layer.

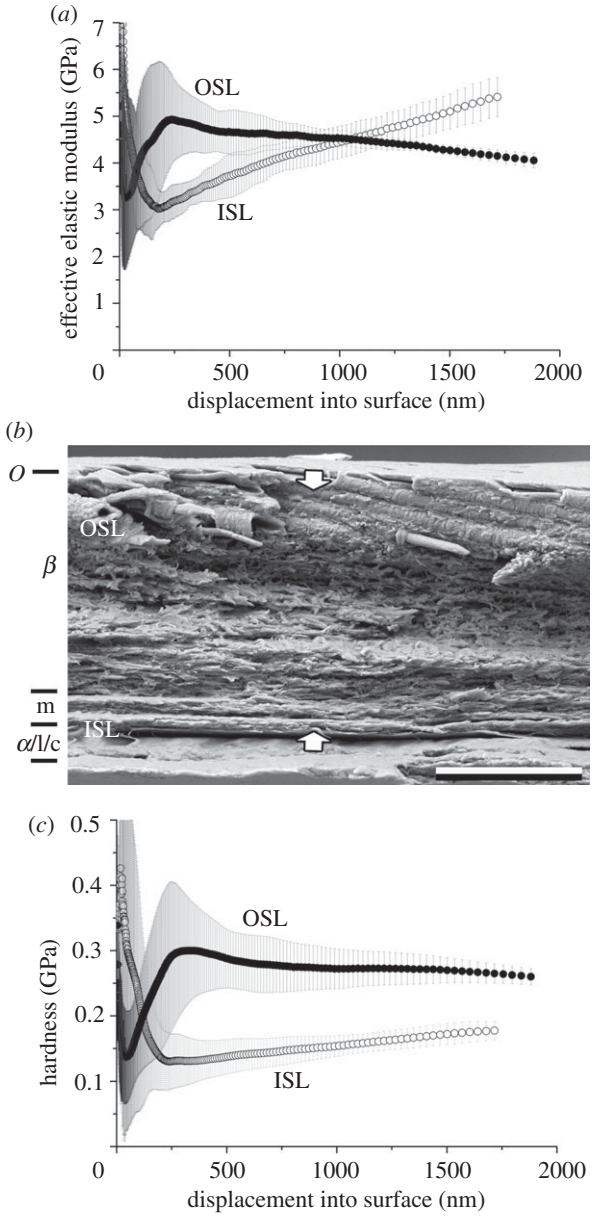

Figure 4. *Lampropeltis getula californiae*. Results of nanoindentation measurements for both the OSL and ISL in relation with the cross-section architecture. (*a*) EEM versus displacement, (*b*) cross-section and (*c*) HD versus displacement. The error bars denote s.d. OSL, outer scale layers; ISL, inner scale layers. The arrows indicate the indentation depth of 2 µm. *O*, *Oberhäutchen*; *β*, β-layer; m, mesos-layer; *α*, α-layer; l, lacunar tissue; c, clear-layer.

3.3. Nanoindentation measurements

Different penetration depths were used for different species in the nanoindentation tests owing to different thickness of their exuvia. Indentation data from the first 7–10% of the total sample thickness can only be used for analysis, in order to avoid the influence of the material properties of the sample holder. Therefore, data were used for penetration depths of 300–1800 nm for *G. colubrinus*, 300–1200 nm for *L. g. californiae*, 300–minimum of 1700 nm for *E. c. cenchria* and 300–1500 nm for *M. viridis*. The results (table 2) show that the OSL is significantly harder and has a higher elasticity modulus, when compared with the ISL ($p < 0.001$, Mann–Whitney rank sum test; *t*-test) in all four species studied.

In order to compare material properties of the inner and outer layers between species, data were selected from the same indentation depths (300–700 nm). Table 3 shows the results of this analysis. The values are all significantly different ($p < 0.001$, Bonferroni *t*-test; *t*-test) between species, except for both the HD and modulus values of the ISL of *L. g. californiae* and *M. viridis* and the HD of the OSL of *L. g. californiae* and *E. c. cenchria*. When comparing the values of the selected indentation depths, as listed earlier, the results between species are also significantly different ($p < 0.001$, Bonferroni *t*-test), with a few

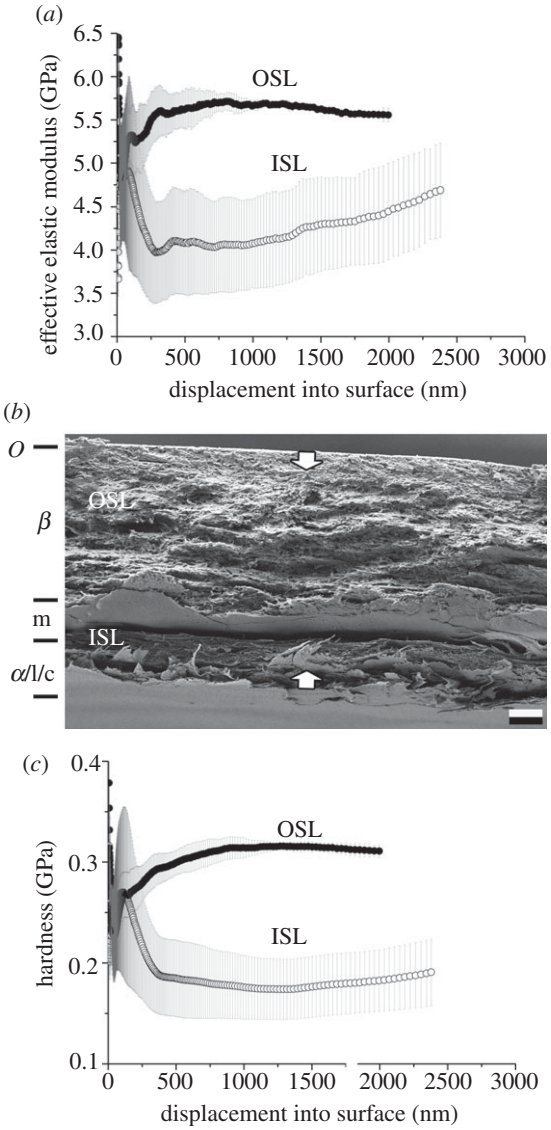

Figure 5. *Epicrates cenchria cenchria*. Results of nanoindentation measurements for both the OSL and ISL in relation with the cross-section architecture. (*a*) EEM versus displacement, (*b*) cross-section and (*c*) HD versus displacement. The error bars denote standard deviations. OSL, outer scale layers; ISL, inner scale layers. The arrows indicate the indentation depth of 2 µm. *O*, *Oberhäutchen*; *β*, β-layer; m, mesos-layer; *α*, α-layer; l, lacunar tissue; c, clear-layer.

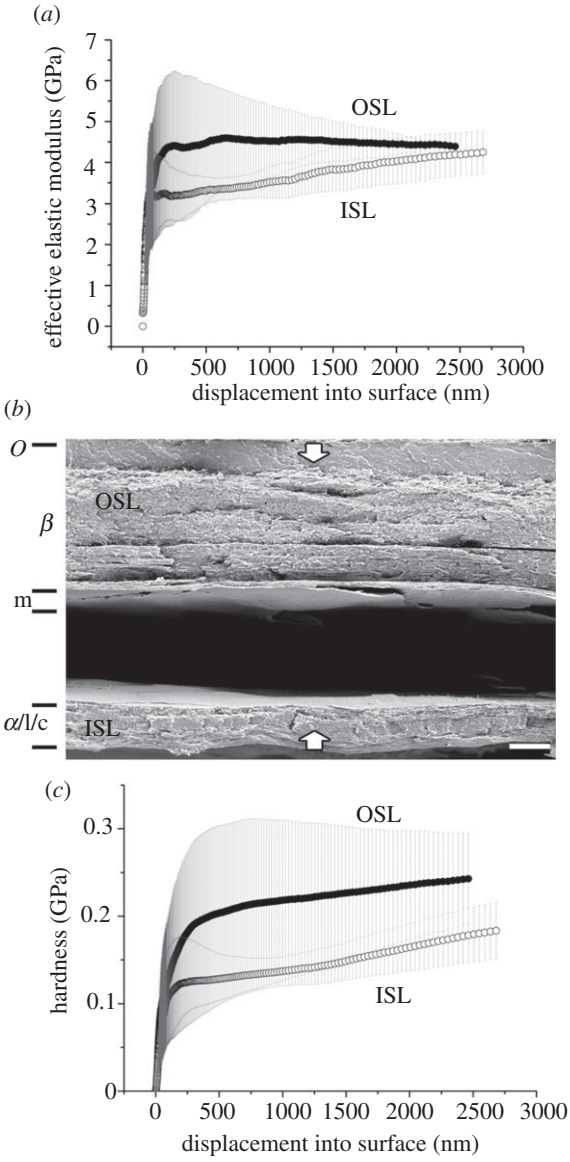

Figure 6. *Morelia viridis*. Results of nanoindentation measurements for both the OSL and ISL in relation with the cross-section architecture. (*a*) EEM versus displacement, (*b*) cross-section and (*c*) HD versus displacement. The error bars denote s.d. OSL, outer scale layers; ISL, inner scale layers. The arrows indicate the indentation depth of 2 µm. *O*, *Oberhäutchen*; *β*, β-layer; m, mesos-layer; *α*, α-layer; l, lacunar tissue; c, clear-layer.

exceptions. As mentioned already, the modulus values of the ISL of *L. g. californiae* and *M. viridis,* and the HD of the OSL of *L. g. californiae* and *E. c. cenchria* are not different. Additionally, the HD values of the ISL of *L. g. californiae* and *G. colubrinus*, as well as the modulus values of the OSL of *E. c. cenchria* and *G. colubrinus* are not different. Even though there is almost always a significant difference between species, the relative values are similar (figure 7).

Tables 4–7 present the comparison in material properties measured at various indentation depths. Three depth intervals were selected. The intervals were not the same for different species, but rather dependant on the exuvium thickness of each species: *G. colubrinus*—400–500, 1200–1300 and 1900–2000 nm (table 4); *L. g. californiae*—300–400, 700–800 and 1100–1200 nm (table 5); *E. c. cenchria*—400–500, 1300–1400; and 1800 to maximum nanometre (table 6), *M. viridis*—300–400, 1000–1100 and 1500–1600 nm (table 7). This comparison revealed a clear trend from soft and flexible inner layers to stiffer and less elastic outer layers for all four species.

In *G. colubrinus* (table 4), there was no significant difference for the HD and modulus values between the three intervals for indentation from the inside of the scale. This would suggest a smooth transition between layers. However, for OSLs, different depth intervals show significant differences in elasticity modulus, and between-depth intervals of 400–500 and 1900–2000 nm in HD.

The modulus and HD values for the ISLs for *L. g. californiae* (table 5) were not significantly

Table 2. Mean and s.d. values of HD and EEM obtained on the inner scale layers (ISL) and outer scale layers (OSL) of the ventral scales of *G. colubrinus* (*G. c.*), *L. g. californiae* (*L. g. c.*), *E. c. cenchria* (*E. c. c.*) and *M. viridis* (*M. v.*) exuvia. Statistical comparison was carried out using one-way RM ANOVA (RM).

	ISL			OSL			
species	measurement	mean (GPa)	s.d. (GPa)	measurement	mean (GPa)	s.d. (GPa)	test
EEM							
G. c.	pooled ($n = 125$)	3.67	0.99	pooled ($n = 79$)	5.85	0.65	RM, $p < 0.01$
L. g. c.	pooled ($n = 140$)	3.32	0.51	pooled ($n = 96$)	5.20	0.73	RM, $p < 0.01$
E. c. c.	pooled ($n = 128$)	4.31	0.76	pooled ($n = 120$)	5.98	0.58	RM, $p < 0.01$
M. v.	pooled ($n = 148$)	3.24	0.72	pooled ($n = 137$)	4.61	0.71	RM, $p < 0.01$
HD							
G. c.	pooled ($n = 125$)	0.16	0.07	pooled ($n = 79$)	0.41	0.07	RM, $p < 0.01$
L. g. c.	pooled ($n = 140$)	0.13	0.03	pooled ($n = 96$)	0.35	0.09	RM, $p < 0.01$
E. c. c.	pooled ($n = 128$)	0.19	0.05	pooled ($n = 120$)	0.33	0.06	RM, $p < 0.01$
M. v.	pooled ($n = 148$)	0.13	0.03	pooled ($n = 137$)	0.19	0.05	RM, $p < 0.01$

Table 3. Comparison of the mean and s.d. values of HD and EEM at the penetration depth of 300–700 nm between *G. colubrinus* (*G. c.*), *L. g. californiae* (*L. g. c.*), *E. c. cenchria* (*E. c. c.*) and *M. viridis* (*M. v.*) for the outer (OSL) and inner scale layers (ISL), respectively. Statistical comparisons were carried out using a Bonferroni *t*-test (T), Mann–Whitney rank sum test (M–W) or *t*-test; n.s.: non-significant difference.

		ISL					OSL				
species		mean (GPa)	s.d. (GPa)	mean (GPa)	s.d. (GPa)	test	mean (GPa)	s.d. (GPa)	mean (GPa)	s.d. (GPa)	test
EEM											
G. c.	*L .g. c.*	3.7	1.1	3.2	0.6	M–W, $p \leq 0.001$	6.4	0.8	5.3	0.8	T, $p \leq 0.001$
	E. c. c.	3.7	1.1	4.4	1.2	M–W, $p \leq 0.001$	6.4	0.8	6.1	1.0	T, $p \leq 0.001$
	M. v.	3.7	1.1	3.2	0.7	M–W, n.s.	6.4	0.8	4.7	0.7	T, $p \leq 0.001$
L .g. c.	*E. c. c.*	3.2	0.6	4.4	1.2	M–W, $p \leq 0.001$	5.3	0.8	6.1	1.0	T, $p = 0.009$
	M. v.	3.2	0.6	3.2	0.7	M–W, $p \leq 0.001$	5.3	0.8	4.7	0.7	T, n.s.
E. c. c.	*M. v.*	4.4	1.2	3.2	0.7	M–W, $p \leq 0.001$	6.1	1.0	4.7	0.7	T, $p = 0.024$
HD											
G. c.	*L .g. c.*	0.17	0.08	0.12	0.03	M–W, $p \leq 0.001$	0.44	0.12	0.36	0.11	T, $p \leq 0.001$
	E. c. c.	0.17	0.08	0.20	0.08	M–W, $p = 0.001$	0.44	0.12	0.34	0.09	T, $p \leq 0.001$
	M. v.	0.17	0.08	0.13	0.04	M–W, n.s.	0.44	0.12	0.20	0.09	T, $p \leq 0.001$
L .g. c.	*E. c. c.*	0.12	0.03	0.20	0.08	M–W, $p \leq 0,.001$	0.36	0.11	0.34	0.09	T, $p = 0.015$
	M. v.	0.12	0.03	0.13	0.04	M–W, $p \leq 0.001$	0.36	0.11	0.20	0.09	T, $p \leq 0.047$
E. c. c.	*M. v.*	0.20	0.08	0.13	0.04	M–W, $p = 0.005$	0.34	0.09	0.20	0.09	T, n.s.

different, except for the HD values between intervals 300–400 and 1100–1200 nm. The HD values for the OSLs were not significantly different between all three depth intervals, whereas the modulus values are significantly different, except for the interval between 300–400 and 1100–1200 nm. The OSLs were inflexible outside becoming more flexible at the indentation depth interval of 700–800 nm, and then become inflexible in the deeper layers of the exuvium. A fine transition of the HD values was observed from the outside to the inside of the exuvium.

The modulus and HD values between the inner and OSLs for *E. c. cenchria* (table 6) were not significantly different, except for the HD values for the OSLs between depth intervals of 400–500 and 1300–1400 nm. It is possible that the indentation depth, selected for this species, was not sufficient to reveal differences between different layers of the exuvium.

The modulus and HD values for the OSLs in *M. viridis* (table 7) were significantly different, except for the HD results between the intervals 1000–1100 and 1500–1600 nm. There was a clear trend from soft and flexible inside layers to hard and inflexible outside ones. The modulus values for the ISLs exhibit a significant difference between the outer and inner most intervals (300–400 and 1500–1600 nm) and not between the others. This implies a smooth transition from the soft to the harder regions. The HD values, on the other hand, for the inner scale values are significantly different, except for the intervals 1000–1100 and 1500–1600 nm, which implies that the interval 300–400 nm is very soft in comparison with the others and that the transition is not very smooth.

4. DISCUSSION

Our morphological results and nanoindenation data obtained on the ventral scales provide strong evidence for the existence of a gradient in material properties

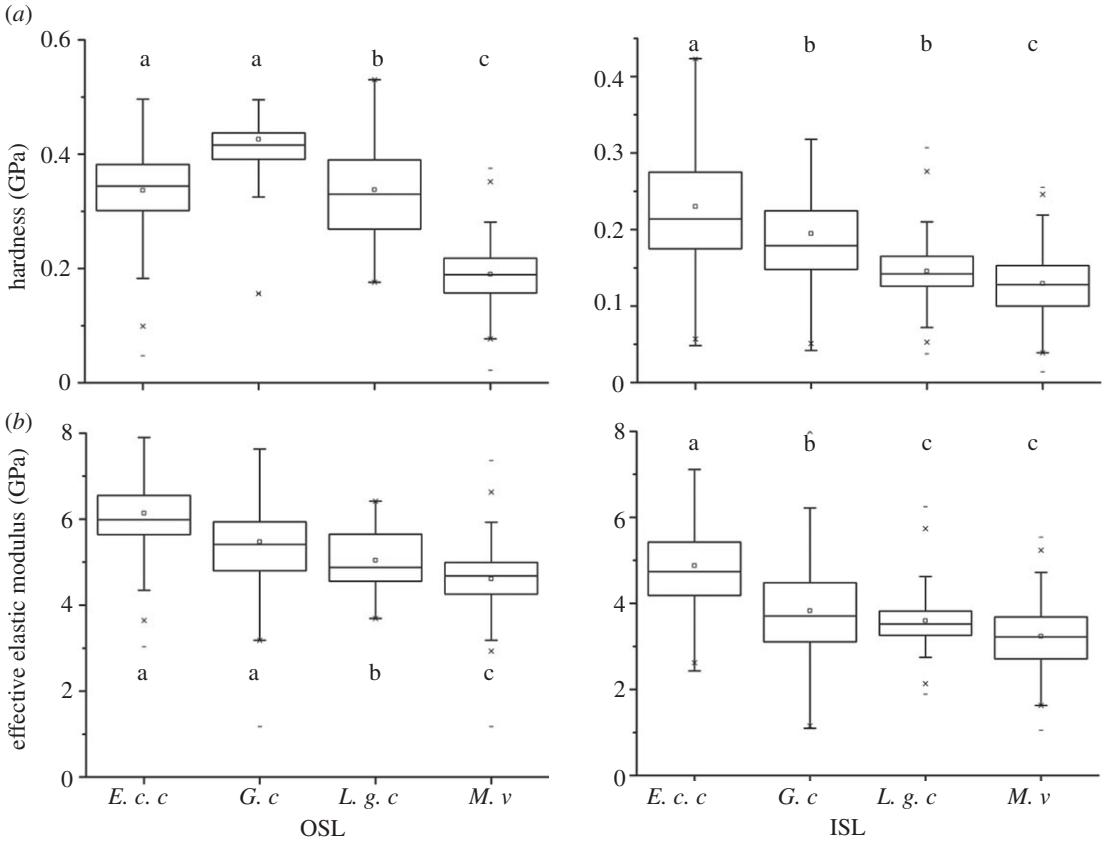

Figure 7. Summary of the (*a*) HD and (*b*) EEM results for penetration depths of 300–1800 nm for *G. colubrinus* (*G. c.*), 300–1200 nm for *L. g. californiae* (*L. g. c.*), 300 nm- minimum of 1700 nm for *E. c. cenchria* (*E. c. c.*) and 300–1500 nm for *M. viridis* (*M. v.*) of the nanoindentation measurements of all four snake species. Statistics: Bonferroni *t*-test.

Table 4. Comparison of the mean and s.d. values measured at three different depth intervals (400–500, 1200–1300 and 1900–2000 nm) of HD and EEM on the outer (OSL) and inner scale layers (ISL) of three *G. colubrinus* scales tested. Statistical comparisons were carried out using Bonferroni *t*-test (T) or one-way RM ANOVA (RM); n.s.: non-significant difference.

depth range (nm)	mean (GPa)	s.d. (GPa)	depth range (nm)	mean (GPa)	s.d. (GPa)	test
EEM						
ISL						
400–500	4.1	0.7	1200–1300	4.0	0.5	RM, n.s.
1200–1300	4.0	0.5	1900–2000	4.4	0.8	RM, n.s.
1900–2000	4.4	0.8	400–500	4.1	0.7	RM, n.s.
OSL						
400–500	6.0	0.9	1200–1300	5.0	0.4	T, $p \leq 0.001$
1200–1300	5.0	0.4	1900–2000	4.5	0.3	T, $p = 0.024$
1900–2000	4.5	0.3	400–500	6.0	0.9	T, $p \leq 0.001$
HD						
ISL						
400–500	0.21	0.05	1200–1300	0.18	0.03	RM, n.s.
1200–1300	0.18	0.03	1900–2000	0.19	0.04	RM, n.s.
1900–2000	0.19	0.04	400–500	0.21	0.05	RM, n.s.
OSL						
400–500	0.39	0.12	1200–1300	0.36	0.05	T, n.s.
1200–1300	0.36	0.05	1900–2000	0.30	0.03	T, n.s.
1900–2000	0.30	0.03	400–500	0.39	0.12	T, $p = 0.003$

in the four snake species studied. The OSLs are harder and exhibit a higher EEM than the inner ones. The results of this study give good support to our previous data on *G. colubrinus* [1]. Interestingly the general trend of the material properties and behaviour of the epidermis for all species studied is achieved differently by using epidermis architecture as a control variable. Because the snake epidermis consists of dead cells or cellular derivatives [51], we can assume no discrepancy in material properties between epidermis of the living

Table 5. Comparison of the mean and s.d. values measured at three different depth intervals (300–400, 700–800 and 1100–1200 nm) of HD and EEM on the outer (OSL) and inner scale layers (ISL) of three *L. g. californiae* scales tested. Statistical comparisons were carried out using a Bonferroni *t*-test (T), Mann–Whitney rank sum test (M–W) or *t*-test; n.s.: non-significant difference.

depth range (nm)	mean (GPa)	s.d. (GPa)	depth range (nm)	mean (GPa)	s.d. (GPa)	test
EEM						
ISL						
300–400	3.3	0.6	700–800	3.8	0.5	T, $p \leq 0.001$
700–800	3.8	0.5	1100–1200	4.2	0.5	T, $p \leq 0.001$
1100–1200	4.2	0.5	300–400	3.3	0.6	T, $p \leq 0.001$
OSL						
300–400	4.5	0.5	700–800	3.8	0.5	*t*-test, $p \leq 0.001$
700–800	3.8	0.5	1100–1200	4.2	0.5	*t*-test, $p = 0.01$
1100–1200	4.2	0.5	300–400	4.5	0.5	*t*-test, n.s.
HD						
ISL						
300–400	0.13	0.04	700–800	0.15	0.03	*t*-test, n.s.
700–800	0.15	0.03	1100–1200	0.16	0.02	*t*-test, n.s.
1100–1200	0.16	0.02	300–400	0.13	0.04	*t*-test, $p = 0.005$
OSL						
300–400	0.27	0.07	700–800	0.25	0.04	*t*-test, n.s.
700–800	0.25	0.04	1100–1200	0.25	0.04	*t*-test, n.s.
1100–1200	0.25	0.04	300–400	0.27	0.07	M–W, n.s.

Table 6. Comparison of the mean and s.d. values measured at three different depth intervals (400–500, 1300–1400 and 1800 max. mm) of HD and EEM on the outer (OSL) and inner scale layers (ISL) of three *E. c. cenchria* scales tested. Statistical comparisons were carried out using a *t*-test, Mann–Whitney rank sum test (M–W) or one-way RM ANOVA (RM); n.s.: non-significant difference.

depth range (nm)	mean (GPa)	s.d. (GPa)	depth range (nm)	mean (GPa)	s.d. (GPa)	test
EEM						
ISL						
400–500	4.2	1.4	1300–1400	4.0	0.8	RM, n.s.
1300–1400	4.0	0.8	1800 to max	4.5	0.7	RM, n.s.
2200 to max.	4.5	0.7	400–500	4.2	1.4	RM, n.s.
OSL						
400–500	6.0	1.0	1300–1400	6.0	0.4	RM, n.s.
1300–1400	6.0	0.4	1800 to max	5.9	0.4	RM, n.s.
1800 to max.	5.9	0.4	400–500	6.0	1.0	RM, n.s.
HD						
ISL						
400–500	0.21	0.11	1300–1400	0.17	0.05	RM, n.s.
1300–1400	0.17	0.05	1800 to max	0.19	0.04	RM, n.s.
2200 to max.	0.19	0.04	400–500	0.21	0.11	RM, n.s.
OSL						
400–500	0.31	0.09	1300–1400	0.35	0.03	*t*-test, n.s.
1300–1400	0.35	0.03	1800 to max	0.35	0.03	*t*-test, n.s.
1800 to max.	0.35	0.03	400–500	0.31	0.09	M–W, n.s.

snake and shed epidermis. Variations in the material properties at different depths may be explained, for instance, by the results of recent ultrastructural studies, showing the existence of three different types of β-keratin and other proteins. These have a temporarily high synthesis rate within the *Oberhäutchen* and β-layer, which decreases in the underlying layers [8,17–19,52].

The HD and modulus values were relatively high close to the surface. Because the tip oscillation (independent of the amplitude) affects the contact formation as well as the contact stabilization for displacements between 0 and approximately 300 nm indentation depth, the results obtained at these shallow depths were not reliable to make any conclusion [1,53].

Previous authors assumed that material properties are important for abrasion resistance [1,4,8,12,40,42,54–57]. It was previously shown that α- and β-keratin differ not only in their distribution within the snake epidermis, but also in their chemical structure [8] and therefore presumably also in material properties [12]. Differences in the chemical structure indicate that the β-keratin molecule may be more stiff and inelastic, when compared

Table 7. Comparison of the mean and s.d. values measured at three different depth intervals (300–400, 1000–1100 and 1500–1600 nm) of HD and EEM on the outer (OSL) and inner scale layers (ISL) of three *M. viridis* scales tested. Statistical comparisons were carried out using a *t*-test or Mann–Whitney rank sum test (M–W); n.s.: non-significant difference.

depth range (nm)	mean (GPa)	s.d. (GPa)	depth range (nm)	mean (GPa)	s.d. (GPa)	test
EEM						
ISL						
300–400	3.3	0.6	1000–1100	3.6	0.4	*t*-test, n.s.
1000–1100	3.6	0.4	1500–1600	3.9	0.4	*t*-test, n.s.
1500–1600	3.9	0.4	300–400	3.3	0.6	*t*-test, $p = 0.003$
OSL						
300–400	5.1	0.2	1000–1100	4.8	0.1	M–W, $p = 0.002$
1000–1100	4.8	0.1	1500–1600	4.6	0.1	*t*-test, $p \leq 0.001$
1500–1600	4.6	0.1	300–400	5.1	0.2	M–W, $p \leq 0.001$
HD						
ISL						
300–400	0.13	0.03	1000–1100	0.15	0.02	*t*-test, n.s.
1000–1100	0.15	0.02	1500–1600	0.16	0.02	*t*-test, $p = 0.006$
1500–1600	0.16	0.02	300–400	0.13	0.03	*t*-test, n.s.
OSL						
300–400	0.24	0.02	1000–1100	0.26	0.01	M–W, $p \leq 0.001$
1000–1100	0.26	0.01	1500–1600	0.27	0.01	M–W, n.s.
1500–1600	0.27	0.01	300–400	0.24	0.02	M–W, $p \leq 0.001$

with α-keratin. That is why it is plausible to assume that materials containing a higher proportion of β-keratin are more robust and therefore posses a stronger resistance against damage. The α-keratin is presumed to provide flexibility to the material of the skin [4,12]. On the basis of the results of Licht & Bennett [55] who studied scaleless snakes, and his own ones, Landmann [4] suggested that the β-layers' main function is to protect the epidermis against abrasion. Later, using nanoindentation, we showed that both the EEM and HD of the OSLs (which are made of β-keratin) is higher compared with the ISLs (which have α-keratin integrated). It was not only experimentally demonstrated that materials containing β-keratin is indeed harder and less stiff than materials containing α-keratin, but that there is a gradient in material properties of the integument from a hard and inflexible outside to a soft and elastic inside [1].

4.1. Material property gradients in other biological tissues

Wang & Weiner [40] as well as Fong *et al.* [56] showed that in the mineralized tissue of the mammalian tooth, layered organization with the gradient of material properties is a key mechanism of the wear resistance. The visible part of the tooth, above the gum, is enveloped by the enamel, which is hard [57] and highly resistant to wear [56]. Its primary function is to protect the underlying dentin (the tooth's major component) and the more flexible, soft pulp [57]. Using indentation tests on pulp and pulpless dog teeth with the Knoop indentor, Fusayama & Maeda [54] showed that the dentin HD in pulpless teeth is lower than that of vital teeth. The authors assume this to be due to the absence of the pulp functioning as a damping layer for the stiffer dentin [54]. Bruet *et al.* [42] used instrumented nanoindenation to measure the multilayered structure of four different organic–inorganic nanocomposite material layers of the scales of the fish Senegal bichir, *Polypterus senegalus*. They could show that the mechanistic origin of penetration resistance include a juxtaposition of multiple distinct reinforcing composite layers. These layers each undergo their own unique deformation mechanisms and regions of differing levels of gradation within and between material layers.

A system that has to endure high amounts of stress under pressure is more effective against abrasion wear, if it has a gradient in structure and properties, because such a design leads to more uniform stress distribution and thus to the minimization of probability of local stress concentration [39,40], which lead to the materials fatigue and failure. Because a hard, inflexible system will break easily under pressure and a flexible system will be easily worn off, the gradient material will improve wear resistance by combining advantages of both stiffness (outside) and flexibility (inside) [1].

4.2. Comparison to other keratinous tissues

The range of mean values of the modulus and HD obtained for the outer (4.6–6.0 GPa, 0.19–0.41 GPa) and ISLs (3.2–4.3 GPa, 0.13–0.19 GPa) are comparable with results, obtained in other studies on the mechanical properties of keratinous materials. The material properties of biological materials, preferably containing either β-keratin ((modulus 1.0–8.0 GPa) [58–61])) or α-keratin ((modulus 3.0–7.5 GPa; HD 0.1–0.4 GPa) [60,62,63]) vary more than would be expected not only because of the testing method used (tensile, bending or nanoindentation tests), but also as a result of different fibre-to-matrix ratios and arrangements of fibres within the matrix. The variability in thickness of the β- and α-keratin layers, as well as the tightness of their packaging is another factor, which may influence the measured modulus. The arrangement and architecture of material, such as that of the snake's

Table 8. Surface, structure and the corresponding environment of the epidermis of *G. colubrinus* (*G. c.*), *L. g. californiae* (*L. g. c.*), *E. c. cenchria* (*E. c. c.*) and *M. viridis* (*M. v.*).

	skin surface	material structure	environment [2,43–45]
G. c.	— little to no microstructure	— layers are dense and differentiated and β-layer with inclusions (20 μm width) — OSL–ISL: 5.9-3.7 GPa e-modulus; 0.4-0.2 GPa hardness	— habitat: burrowing; desert — substrate: sand — locomotion: lateral undulation on sand; in sand unknown
L. g. c.	— sharp, relatively long and regular, densely packed denticulations — longitudinal pits	— loosely packed cells with fibres in the β-layer (9 μm) — OSL–ISL: 5.2-3.3 GPa e-modulus; 0.4-0.1 GPa hardness	— habitat: terrestrial; woods, scrubs and cultivated land in the southern USA — substrate: sand, rocks, branches, leaves, etc. — locomotion: lateral undulation
E. c. c.	— denticulation pattern, without elevations — long longitudinal grooves and round regular pits	— spongy, fraying, dense cells (40 μm) — OSL–ISL: 6.0-4.3 GPa e-modulus; 0.3-0.2 GPA hardness	— habitat: generalist; tropical rainforest — substrate: tress, rocks, water, etc. — locomotion: rectilinear, lateral undulation
M. v.	— regular, finger-like denticulations — few round, irregular pits	— cell types specifically merge to one mass (12 μm) — OSL–ISL: 4.6-3.2 GPa e-modulus; 0.2-0.1 GPa hardness	— habitat: trees; tropical rainforest — substrate: trees — locomotion: lateral undulation

integument (relatively tight packaging of layers) or the bird feather (hollow feather shaft), influences material properties and is related to the specific function of the material. For example, Bonser [59] found that the rachis of two different feather types (modulus: wing feather, 1.7 GPa and body contour feather, 2.4 GPa) of the ostrich revealed two significantly different moduli, depending on the mechanical loads to which the feathers are subjected. Astbury & Bell [64] state that the feather geometry and the material ultrastructure are important features in determining the mechanical behaviour of a whole feather. In the present study, it is shown that despite a variation in layer thickness and overall epidermis thickness, HD and stiffness measurements for all four species tested lead to similar results for the HD and modulus values for the ISL and OSL (penetration depths of 300–700 nm). Perhaps this is an optimal range of values, which might reflect an adaptation for sliding locomotion.

4.3. Mechanical behaviour

Even though the properties of the epidermis material are similar, differences in epidermis thickness, scale size and shape of the microstructure may lead to a very different friction and wear behaviour. This in turn may lead to an adaptation to specific habitat and to the locomotion on specific substrates. In general, two samples of the same material with different thicknesses will show different mechanical behaviour on the same substrate. The thicker sample will show less abrasive wear than the thinner sample, because the energy introduced into the system during shear is dissipated in deformations of the bulk supporting layer. In the thinner sample, shear stress will be less dissipated because of lacking supportive layers and therefore a larger proportion of shear stress will cause abrasion. The thickness of the epidermis with its specific mechanical material properties may represent a variable for optimization for abrasion resistance on a preferable substrate in different snake species. The epidermis of the four snake species tested exhibits similar material properties even though epidermis layering is different. In artificially produced materials, various material properties may be created by the reinforcement with stiffer fibres or by developing a higher number of layers with different composition or properties [65–68]. The epidermis layers consist of varying cell types, depending on the species. For instance, when comparing the *Oberhäutchen* and β-layer, *G. colubrinus* has a relatively thin OSL in relation to the entire epidermis, which is densely packed and has inclusions of granular/vesicular nature (figure 3*b*); *L. g. californiae* has a relatively thick OSL with fibre filaments arranged into the longitudinal direction of the body axis; OSL in *E. c. cenchria* is relatively homogeneous and thick consisting of frayed and brittle cells, in which only the *Oberhäutchen* can be differentiated; and the OSL of *M. viridis* consists of a homogeneous, spongy cell cluster. A variation in epidermis layering and surface microstructure may lead to a variation in the canalization of shear forces and, therefore, in different wear behaviour [66,69].

Specific epidermis architecture may cause force redistribution and canalization. For instance, fractures caused by forces exerted on a composite material will most probably be channelled and ultimately stopped at interfaces, in contrast to bulk materials [70]. The crack propagation is also dependent on the stiffness of the material: the stiffer the material, the larger the fracture velocity, because exerted energy cannot be dissipated into deformations.

The differing architecture of the epidermis of the four species studied may correlate with a specific adaptation to factors such as habitat, substrate and locomotion. Locomotion type and velocity in snakes is

probably dependent not only on species or body mass, but also on substrate conditions, which in turn is likely to be influenced through the habitat. A tree-climbing snake in a tropical habitat (high humidity and temperature), such as *M. viridis,* will probably have different mechanical forces acting upon the skin, compared with a sand-swimming, desert snake, such as *G. colubrinus* (table 8).

4.4. Role of fillers/inclusions

The reinforcement of polytetrafluoroethylene (PTFE) by carbon fibres with an elastic modulus of 370 GPa increases the elastic modulus of PTFE from 3.2 to 45 GPa [65]. The fibre reinforcement and the grain inclusion in the OSL of *L. g. californiae* and *G. colubrinus,* respectively, may also provide the material adaptation leading to a lower degree of abrasion. Material properties of the skin of the snakes studied (OSL–ISL: 4.6–6.0–3.2–4.3 GPa effective e-modulus) are in the range of that of some polymers (e-modulus: nylon 2.5 GPa, PTFE 3.2 GPa, polystyrene 3–3.5 GPa, polypropylene 1.5–2 GPa, polyethylene terephthalate 2–2.7 GPa [65,71,72]. These polymers usually exhibit low friction, compared with metals, but moderate wear, which is why polymers are often impregnated with fibres, such as carbon graphite or glass and powders (graphite, MoS_2, bronze and PTFE) [73]. Lancaster [65] showed that not only friction is reduced by adding carbon fibres to polymers, but that also the rate of wear is reduced. The author proposes that these phenomena occur independently of the matrix material. Polymer fillers that are stiffer than the polymer itself will probably lead to specific canalization of wear, because the surface mainly deforms between the fibre fillers.

4.5. Surface anisotropy

Surface anisotropy may additionally influence redistribution and canalization of contact forces during sliding on the substrate. Specific surface microstructure may lead to different abrasion quality and canalization of scratches in one particular direction. In this case, generation of new scratches might even be responsible for sustaining the anisotropic microstructure for some period of time. Because scales of different snakes exhibit different surface microstructures, both the abrasion quality and its magnitude may also be dependent on the specific geometry of the microstructure. Distinct denticulations found on the ventral scales of *L. g. californiae* presumably lead to canalization of forces, resulting in scratches in longitudinal direction. Such longitudinal grooves generally lead to a lower initial and steady-state wear, if compared with transverse grooves [73]. Canalization will probably not be exhibited on scales with little to no surface structure, such as the ventral scales of *G. colubrinus*. Here, shallow but numerous scratches without a specific orientation are observed.

5. CONCLUSION AND OUTLOOK

Data of our study show, for the first time, the HD and EEM values at different depths of the ventral skin of four snake species. The comparison of the surface microstructure and material architecture demonstrated a gradient in material properties of the integument from a hard and inflexible outside to a soft and elastic inside. This feature is assumed to be a functional mechanism explaining abrasion resistance of the skin material. An additional mechanism might be the presence of surface microstructure, canalizing wear in the longitudinal direction. The variety in skin architecture found for the four snake species studied may represent an adaptation to a specific habitat.

Comparative studies of the epidermis ultrastructure by using transmission electron microscopy (TEM), as well as the local experimental testing of the skin wear, might aid in the understanding of the role of structural features in abrasion reduction of the snake epidermis.

The experiments comply with the 'Principles of animal care' (publication no. 86–23, revised 1985) of the National Institute of Health, and also with the current laws of Germany.

This study was supported by the Federal Ministry of Education, Science and Technology, Germany (BMBF project Biona 01RB0812A) and by the German National Merit Foundation. Animal care at the University of Kiel was provided by S. Bootsmann, S. Holz, T. Arp and M. Eschke. Figure 1*a* was reproduced/adapted with permission from the Journal of Experimental Biology, Barbakadze, N., Enders, S., Gorb, S. & Arzt, E. 2006 Local mechanical properties of the head articulation cuticle in the beetle *Pachnoda marginata* (Coleoptera: Scarabaeidae). *J. Exp. Biol.* **209**, 722–730.

REFERENCES

1 Klein, M.-C., Deuschle, J. & Gorb, S. 2010 Material properties of the skin of the Kenyan sand boa *Gongylophis colubrinus* (Squamata, Boidae). *J. Comp. Physiol. A* **196**, 659–668. (doi:10.1007/s00359-010-0556-y)
2 Mattison, C. 1995 *The encyclopedia of snakes.* London, UK: Cassel & Co.
3 Baden, H. P. & Maderson, P. F. A. 1970 Morphological and biophysical identification of fibrous proteins in the amniote epidermis. *J. Exp. Zool.* **174**, 225–232. (doi:10.1002/jez.1401740211)
4 Landmann, L. 1979 Keratin formation and barrier mechanisms in the epidermis of *Natrix natrix* (Reptilia: Serpentes): an ultrastructural study. *J. Morphol.* **162**, 93–126. (doi:10.1002/jmor.1051620107)
5 Barbakadze, N., Enders, S., Gorb, S. & Arzt, E. 2006 Local mechanical properties of the head articulation cuticle in the beetle *Pachnoda marginata* (Coleoptera, Scarabaeidae). *J. Exp. Biol.* **209**, 722–730. (doi:10.1242/jeb.02065)
6 Landmann, L. 1986 Biology of the integument. In *The skin of reptiles, epidermis and dermis* (eds J. Bereither-Hahn & G. A. Matoltsy & K. Sylvia-Richards), ch. 9, pp. 150–185. Heidelberg, Germany: Springer.
7 Maderson, P. F. A., Rabinowitz, T., Tandler, B. & Alibardi, L. 1998 Ultrastructural contributions to an understanding of the cellular mechanisms involved in lizard skin shedding with comments on the function and evolution of a unique lepidosaurian phenomenon. *J. Morphol.* **236**, 1–24. (doi:10.1002/(SICI)1097-4687(199804)236:1<1::AID-JMOR1>3.0.CO;2-B)
8 Toni, M. & Alibardi, L. 2007 Alpha- and beta-keratin of the snake epidermis. *Zoology* **110**, 41–47. (doi:10.1016/j.zool.2006.07.001)

9 Mercer, E. H. 1961 *Keratin and keratinization*. Oxford, UK: Pergamon Press, Inc.
10 Maderson, P. F. A. 1964 The skin of lizards and snakes. *J. Herpet* **3**, 151–154.
11 Alexander, N. J. 1970 Comparison of α and β keratin in reptiles. *Z. Zellforsch.* **110**, 153–165.
12 Matoltsy, A. G. 1976 Keratinization. *J. Invest. Dermatol.* **67**, 20–25. (doi:10.1111/1523-1747.ep12512473)
13 Wyld, J. A. & Brush, A. H. 1979 The molecular heterogeneity and diversity of reptilian keratins. *J. Mol. Evol.* **12**, 331–347. (doi:10.1007/BF01732028)
14 Fuchs, E. & Marchuk, D. 1983 Type I and type II keratins have evolved from lower eukaryotes to from the epidermal intermediate filaments in mammalian skin. *Proc. Natl Acad. Sci. USA* **80**, 5857–5861. (doi:10.1073/pnas.80.19.5857)
15 Carver, W. E. & Sawyer, R. H. 1987 Development and keratinization of the epidermis in the common lizard, *Anolis carolinensis*. *J. Exp. Zool.* **243**, 435–443. (doi:10.1002/jez.1402430310)
16 O'Guin, W. M., Galvin, S., Schermer, A. & Sun, T. T. 1987 Patterns of keratin expression define distinct pathways of epithelial development and differentiation. *Curr. Top. Dev. Biol.* **22**, 97–125. (doi:10.1016/S0070-2153(08)60100-3)
17 Alibardi, L. & Toni, M. 2006 Cytochemical, biochemical and molecular aspects of the process of keratinization in the epidermis of reptilian scales. *Prog. Histochem. Cytochem.* **40**, 73–134. (doi:10.1016/j.proghi.2006.01.001)
18 Alibardi, L. & Toni, M. 2006 Immunological characterization and fine localization of lizard beta-keratin. *J. Exp. Zool.* **306B**, 528–538. (doi:10.1002/jez.b.21105)
19 Alibardi, L. & Toni, M. 2006 Immunolocalization and characterization of beta-keratins in growing epidermis of chelonians. *Tissue Cell* **38**, 53–63. (doi:10.1016/j.tice.2005.11.001)
20 Arzt, E., Enders, S. & Gorb, S. 2002 Towards a micromechanical understanding of biological surface devices. *Z. Met.kd.* **93**, 345–351.
21 Enders, S., Barbakadze, N., Gorb, S. N. & Arzt, E. 2004 Exploring biological surfaces by nanoindentation. *J. Mater. Res.* **19**, 880–887. (doi:10.1557/jmr.2004.19.3.880)
22 Leydig, F. 1868 *Ueber Organe eines sechsten Sinnes. Zugleich als Beitrag zur Kenntniss des feineren Baues der Haut bei Amphibien und Reptilien*. Dresden, Germany: E. Blochmann & Sohn.
23 Leydig, F. 1873 Ueber die äusseren Bedeckungen der Reptilien und Amphibien. *Archiv fuer Mikroskopische Anatomie* **9**, 753–794. (doi:10.1007/BF02956189)
24 Picado, C. 1931 Epidermal microornamentations of the Crotalinae. *Bull. Antivenin Inst. Am.* **4**, 104–105.
25 Hoge, A. R. & Souza Santos, P. 1953 Submicroscopic structure of 'stratum corneum' of snakes. *Science* **118**, 410–411. (doi:10.1126/science.118.3067.410)
26 Price, R. M. 1982 Dorsal snake scale microdermatoglyphics: ecological indicator or taxonomic tool. *J. Herpetol.* **16**, 294–306. (doi:10.2307/1563721)
27 Price, R. & Kelly, P. 1989 Microdermatoglyphics: basal patterns and transition zones. *J. Herpetol.* **23**, 244–261. (doi:10.2307/1564446)
28 Gower, D. J. 2003 Scale microornamentation of uropeltid snakes. *J. Morphol.* **258**, 249–268. (doi:10.1002/jmor.10147)
29 Schmidt, C. V. & Gorb, S. N. 2012 Snake scale microstructure: phylogenetic significance and functional adaptations. Stuttgart, Germany: Schweizerbart Science Publishers.
30 Berthé, R. A., Wetshoff, G., Bleckmann, H. & Gorb, S. N. 2009 Surface structure and frictional properties of the Amazon tree boa *Corallus hortulanus* (Squamata, Boidae). *J. Comp. Physiol. A* **195**, 311–318. (doi:10.1007/s00359-008-0408-1)
31 Hazel, J., Stone, M., Grace, M. S. & Tsukruk, V. V. 1999 Nanoscale design of snake skin for reptation locomotions via friction anisotropy. *J. Biomech.* **32**, 477–484. (doi:10.1016/S0021-9290(99)00013-5)
32 Abdel-Aal, H. A., Mansori, M. E. & Mezghani, S. 2010 Multi-scale investigation of surface topography of ball python (*Python regius*) shed skin in comparison to human skin. *Tribol. Lett.* **37**, 517–527. (doi:10.1007/s11249-009-9547-y)
33 Amemiya, F., Goris, R. C., Masuda, Y., Kishida, R., Atobe, Y., Ishii, N. & Kusunoki, T. 1995 The surface architecture of snake infrared receptor organs. *Biomed. Res.* **16**, 411–421.
34 Amemiya, F., Goris, R. C., Atobe, Y., Ishii, N. & Kusunoki, T. 1996 The ultrastructure of infrared receptors in a boid snake, *Python regius*: evidence for periodic regeneration of the terminals. *Anim. Eye Res.* **15**, 13–25.
35 Amemiya, F., Ishiki, T., Goris, R. C., Atobe, Y. & Kusunoki, T. 1996 Ultrastructure of the crotaline snake infrared pit receptors: SEM confirmation of TEM findings. *Anat. Rec.* **246**, 135–146. (doi:10.1002/(SICI)1097-0185 (199609)246:1<135::AID-AR15>3.0.CO;2-Q)
36 Campbell, A. L., Bunning, T. J., Stone, M. O., Church, D. & Grace, M. S. 1999 Surface ultrastructure of pit organ, spectacle, and non pit organ epidermis of infrared imaging boid snakes: a scanning probe and scanning electron microscopy study. *J. Struct. Biol.* **126**, 105–120. (doi:10.1006/jsbi.1999.4121)
37 Fuchigami, N., Hazel, J., Gorbunov, V. V., Stone, M., Grace, M. & Tsukruk, V. V. 2001 Biological thermal detection in infrared imaging snakes. I. Ultramicrostructure of pit receptor organs. *Biomacromolecules* **2**, 757–764. (doi:10.1021/bm015537z)
38 Gorbunov, V., Fuchigami, N., Stone, M., Grace, M. & Tsukruk, V. V. 2002 Biological thermal detection: micromechanical and microthermal properties of biological infrared receptors. *Biomacromolecules* **3**, 106–115. (doi:10.1021/bm015591f)
39 Gibson, L. J. & Ashby, M. F. 1988 *Cellular solids: structures and properties*. New York, NY: Pergamon Press.
40 Wang, R. Z. & Weiner, S. 1998 Strain–structure relations in human teeth using Moire fringes. *J. Biomech.* **31**, 135–141. (doi:10.1016/S0021-9290(97)00131-0)
41 Suresh, S. 2001 Graded materials for resistance to contact deformation and damage. *Science* **292**, 2447–2451. (doi:10.1126/science.1059716)
42 Bruet, B. J. F., Song, J., Boyce, M. C. & Ortiz, C. 2008 Materials design principles of ancient fish armour. *Nat. Mat.* **7**, 1–9. (doi:10.1038/nmat2231)
43 Mattison, C. 1999 *Schlangen. Die interessantesten Arten der Welt*. London, UK: Dorling Kindersley.
44 Greene, H. W. 1997 *Snakes: the evolution of mystery in nature*. London, UK: University of California Press.
45 Schmidt, D. 2004 *Die Kettennatter. Lampropeltis getula*. Münster, Germany: Natur und Tier-Verlag GmbH.
46 Deuschle, J., Enders, S. & Arzt, E. 2007 Surface detection in nanoindentation of soft polymers. *J. Mater. Res.* **22**, 3107–3119. (doi:10.1557/JMR.2007.0394)
47 Oliver, W. C. & Pharr, G. M. 1992 An improved technique for determining hardness and elastic modulus using load and displacement sensing indentation experiments. *J. Mater. Res.* **7**, 1564–1583. (doi:10.1557/JMR.1992.1564)
48 Xu, H. H. K., Smith, D. T., Jahanmir, S., Romber, E., Kelly, J. R., Thompson, V. P. & Rekow, E. D. 1998 Indentation damage and mechanical properties of human enamel and dentin. *J. Dent. Res.* **77**, 472–480. (doi:10.1177/00220345980770030601)

49 Ebenstein, D. M. & Pruitt, L. A. 2006 Nanoindentation of biological materials. *Nano Today* **1**, 26–33. (doi:10.1016/S1748-0132(06)70077-9)

50 Oliver, W. C. & Pharr, G. M. 2004 Measurement of hardness and elastic modulus by instrumented indentation: advances in understanding and refinements to methodology. *J. Mater. Res.* **19**, 3–20. (doi:10.1557/jmr.2004.19.1.3)

51 Irish, F. J., Williams, E. E. & Seling, E. 1988 Scanning electron microscopy of changes in the epidermal structure occurring during the shedding cycle in squamate reptiles. *J. Morphol.* **197**, 105–126. (doi:10.1002/jmor.1051970108)

52 Dalla Valle, L., Toffolo, V., Belvedere, P. & Alibardi, L. 2005 Isolation of mRNA encoding a glycine-proline-rich β-keratin expressed in the regenerating epidermis of lizard. *Dev. Dyn.* **234**, 934–947. (doi:10.1002/dvdy.20581)

53 Deuschle, J. 2008 Mechanics of soft polymer indentation. Dissertation, Max-Planck-Institute for Metals Research Stuttgart and Institute for Metallography of the University of Stuttgart, Germany.

54 Fusayama, T. & Maeda, T. 1968 Effect of pulpectomy on dentin hardness. *J. Dent. Res.* **48**, 452–460. (doi:10.1177/00220345690480032201)

55 Licht, P. & Bennett, A. F. 1972 A scaleless snake: tests of the role of reptilian scales in water loss and heat transfer. *Copeia* **4**, 702–707. (doi:10.2307/1442730)

56 Fong, H., Sarikaya, M., White, S. N. & Snead, M. L. 2000 Nano-mechanical properties profiles across dentin–enamel junction of human incisor teeth. *Mat. Sci. Eng.* **7**, 119–128. (doi:10.1016/S0928-4931(99)00133-2)

57 Zheng, J., Zhou, Z. R., Zhang, J., Li, H. & Yu, H. Y. 2003 On the friction and wear behaviour of human tooth enamel and dentin. *Elsevier Wear* **255**, 967–974. (doi:10.1016/S0043-1648(03)00079-6)

58 Bonser, R. H. C. & Purslow, P. P. 1995 The Young's modulus of feather keratin. *J. Exp. Biol.* **198**, 1029–1033.

59 Bonser, R. H. C. 2001 The elastic properties of wing and contour feather keratin from the ostrich *Struthio camelus*. *Ibis* **143**, 144–145. (doi:10.1111/j.1474-919X.2001.tb04178.x)

60 Moran, P., Towler, M. R., Chowdhury, S., Saunders, J., German, M. J., Lawson, N. S., Pollock, H. M., Pillay, L. & Lyons, D. 2007 Preliminary work on the development of a novel detection method for osteoporosis. *J. Mater. Sci.* **18**, 969–974. (doi:10.1007/s10856-006-0037-6)

61 Huber, G., Orso, S., Spolenak, R., Wegst, U. G. K., Enders, S., Gorb, S. N. & Arzt, E. 2008 Mechanical properties of a single gecko seta. *Int. J. Mater. Res.* **2008**, 1113–1118. (doi:10.3139/146.101750)

62 Farren, L., Shayler, S. & Ennos, A. R. 2004 The fracture properties and mechanical design of human fingernails. *J. Exp. Biol.* **207**, 735–741. (doi:10.1242/jeb.00814)

63 Wei, G., Bhushan, B. & Torgerson, P. M. 2005 Nanomechanical characterization of human hair using nanoindentation and SEM. *Elsevier Ultramicroscopy* **105**, 248–266. (doi:10.1016/j.ultramic.2005.06.033)

64 Astbury, W. T. & Bell, F. O. 1939 X-ray data on the structure of natural fibres and other bodies of high molecular weight. *Tabulae Biol.* **17**, 90–112.

65 Lancaster, J. K. 1968 The effect of carbon fibre reinforcement on the friction and wear of polymers. *Br. J. Appl. Phys.* **1**, 549–559.

66 Dayong, H. & Jiang, D. 1993 The elastic modulus of filled polymer composites. *J. Appl. Poly. Sci.* **49**, 617–621. (doi:10.1002/app.1993.070490408)

67 Hak, G. L., Hwang, H. Y. & Lee, D. G. 2006 Effect of wear debris on the tribological characteristics of carbon fiber epoxy composites. *Elsevier Wear* **261**, 453–459. (doi:10.1016/j.wear.2005.12.012)

68 Basavarajappa, S., Arun, K. V. & Davim, J. P. 2009 Effect of filler materials on dry sliding wear behavior of polymer matrix composites—a taguchi approach. *J. Min. Mat. Charact. Eng.* **8**, 379–391. (doi:10.4236/jmmce.2009.85034)

69 Sidorenko, A., Ahn, H.-S., Kim, D.-I., Yang, H. & Tsukruk, V. V. 2002 Wear stability of polymer nanocomposite coatings with trilayer architecture. *Elsevier Wear* **252**, 946–955.

70 Matthews, F. L. & Rawlings, R. D. 1999 *Composite materials: engineering and science*. Boca Raton, FL: CRC Press.

71 The Engineering ToolBox. Material properties, polymers 2012 See http://www.engineering toolbox.com (retrieved: 22 April 2012). Arlington, USA.

72 MatWeb Material property data. 2012 See http://www.matweb.com (retrieved: 22 April 2012). Blacksburg, USA.

73 Bhushan, B. 2002 *Introduction to tribology*. New York, NY: John Wiley & Sons, Inc.